Author(s): Ugartemendia, Andoni; Mercero, Jose M.; de Cózar, Abel; Melander, Marko M.; Akola, Jaakko; Jimenez-Izal, Elisa

Title: Deposited PtGe clusters as active and durable catalysts for CO oxidation

Ugartemendia, A., Mercero, J. M., de Cózar, A., Melander, M. M., Akola, J., & Jimenez-Izal, E. (2024). Deposited PtGe clusters as active and durable catalysts for CO oxidation. ChemCatChem, 16(3), Article e202301137. https://doi.org/10.1002/cctc.202301137

ChemCatChem

Research Article
doi.org/10.1002/cctc.202301137

Chemistry Europe
European Chemical Societies Publishing

www.chemcatchem.org

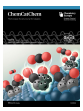

Deposited PtGe Clusters as Active and Durable Catalysts for CO Oxidation**

Andoni Ugartemendia,[a] Jose M. Mercero,*[a] Abel de Cózar,[b, c] Marko M. Melander,[d] Jaakko Akola,*[e, f] and Elisa Jimenez-Izal*[a, c]

Control of CO emissions raises serious environmental concerns in the current chemical industry, as well as in nascent technologies based on hydrogen such as electrolyzers and fuel cells. As for now, Pt remains one of the state-of-the-art catalysts for the CO oxidation reaction, but unfortunately, it suffers from CO self-poisoning. Recently, Pt–Ge alloys were proposed to be an excellent alternative to reduce CO poisoning. This work investigates the impact of Ge content on the CO oxidation kinetics of Pt_4Ge_n subnanoclusters supported on MgO. A Ge concentration dependence of the reaction kinetics is found due to a strong synergy between Pt and Ge. Pt–Ge nanoalloys act as a bifunctional catalyst by displaying dual adsorption sites; i.e., CO is adsorbed on Pt whereas oxygen binds to Ge, forming an alternative oxygen source GeO_x. Besides, Ge alloying modifies the electronic structure of Pt (ligand effects) and reduces the affinity to CO. In this way, the competition between CO and O_2 adsorption and the overbinding of CO is alleviated, achieving a CO poisoning-free kinetic regime. Our calculations suggest that Pt_4Ge_3 is the optimal catalyst, evidencing that alloying composition is a parameter of extreme importance in nanocatalyst design. The work relies on global optimization search techniques to determine the accessibility of multiple structures at different conditions, mechanistic studies and microkinetic modeling.

Introduction

Carbon monoxide (CO) is an odorless gas which is extremely hazardous for health and the environment. It is usually produced as a result of the incomplete combustion of hydrocarbon compounds. Thus the catalytic oxidation of CO has become a crucial step for the control of CO emissions in a wide range of processes, such as vehicle exhaust treatment and purification of hydrogen for fuel cell applications. Moreover, due to its simplicity, CO oxidation is used as a probe reaction to model more complex reactions such as the Fischer-Tropsch synthesis.[1–3]

Platinum group metals (PGMs) including Pt, Pd, Rh, *etc.* are widely known for their excellent catalytic activity for many reactions of critical importance such as CO oxidation.[4] Catalyst nanoparticles (NPs) are usually stabilized by dispersion over metal-oxide supports in industrial applications.[5] CO oxidation usually displays bistable kinetics over Pt.[6] At low temperature and/or low O_2 pressure, it suffers from CO self-poisoning (chemical deactivation), slowing down the reaction rate. The catalyst surface is then saturated with a CO layer that prevents the coadsorption of O_2. Therefore, there are not enough free active sites in which the O_2 molecules can impinge and react with the coadsorbed CO, and the catalyst is rendered totally

[a] *A. Ugartemendia, Prof. J. M. Mercero, Prof. E. Jimenez-Izal*
Polimero eta Material Aurreratuak: Fisika, Kimika eta Teknologia Saila
Kimika Fakultatea
Euskal Herriko Unibertsitatea (UPV/EHU) and Donostia International Physics Center (DIPC)
20018 Donostia, Euskadi (Spain)
E-mail: jm.mercero@ehu.es
elisa.jimenez@ehu.es

[b] *Prof. A. de Cózar*
Kimika Organiko I Saila
Kimika Fakultatea
Euskal Herriko Unibertsitatea (UPV/EHU) and Donostia International Physics Center (DIPC)
20018 Donostia, Euskadi (Spain)

[c] *Prof. A. de Cózar, Prof. E. Jimenez-Izal*
IKERBASQUE
Basque Foundation for Science
Bilbao, 48009 Euskadi (Spain)

[d] *Dr. M. M. Melander*
Department of Chemistry
Nanoscience Center
University of Jyväskylä
FI-40014 Jyväskylä (Finland)

[e] *Prof. J. Akola*
Department of Physics
Norwegian University of Science and Technology (NTNU)
NO-7491 Trondheim (Norway)
E-mail: jaakko.akola@ntnu.no

[f] *Prof. J. Akola*
Computational Physics Laboratory
Faculty of Engineering and Natural Sciences
Tampere University
FI-33014 Tampere (Finland)

[**] *A previous version of this manuscript has been deposited on a preprint server (https://doi.org/10.26434/chemrxiv-2023-lfws6).*

Supporting information for this article is available on the WWW under https://doi.org/10.1002/cctc.202301137

inactive after solely a few number of catalytic cycles, costing billions of dollars annually in the industry.[7,8] At high temperature and/or high O_2 pressure on the other hand, a first order kinetic phase transition (*i.e.*, alteration of the adsorbates adsorption-desorption equilibrium) occurs leading to a more reactive state. Now, the adsorbed CO reacts immediately increasing the CO_2 formation rate and dissociated O becomes the predominant species. Since high temperature favors catalyst deactivation due to sintering and coking, CO poisoning imposes severe constraints over the maneuverability of the optimal operating reaction conditions. This scenario together with the high cost and limited availability of Pt hampers its use in large-scale production.

Subnanometer clusters have attracted a widespread attention in the last decades since they show unique catalytic properties compared with larger NPs due to finite-size effects.[9–12] In this regime the catalytic properties become size dependent to the extreme that the addition or subtraction of a single atom can have a drastic impact on them; this is the regime where each atom counts.[13,14] More importantly, they possess a huge surface to volume ratio which allows a maximal utilization of atoms, *i.e.*, the so-called atomic efficiency. It is important to note that, treating clusters as static structures has been shown to be a simplified picture.[15–17] In reality, clusters display high fluxionality at usual operating temperatures and form an ensemble of statistically relevant isomers, each of which exhibits different catalytic properties and constantly interconverting in response to external stimuli. All in all, clusters present a very strong structure-activity relationship by which the catalytic properties can be tuned by physical and chemical modifications (*e.g.*, size, composition, support, ligand capping, *etc.*); in short, clusters offer a myriad of possibilities for nanocatalyst design.

Alloying the catalyst with an ancillary element is a promising strategy to mitigate CO poisoning.[18] One of the advantages of this strategy is that it allows a reduction in the Pt loading, making them more attractive for commercialization. It is desirable that the bimetallic catalyst should maintain at least the same catalytic activity as Pt, as well as improve the selectivity towards different poisons. Several Pt-based bimetallic systems have been found in the last years for CO oxidation. For instance, Pt–Ni/γ-Al_2O_3,[19] Pt–Fe/GA,[20] Pt–Fe/γ-Al_2O_3,[21] Pt–Sn/AC,[22,23] Pt–Ru/SiO_2[24] and Pt–Re/SiO_2[25] outperform their monometallic counterparts with higher CO conversion rates. The enhancement of the bimetallic catalysts is usually ascribed to ligand (electronic) and/or bifunctional effects. Ligand effects occur when the alloying element modifies the Pt electronic structure (*e.g.*, electron donation and back-donation capacity of Pt) without directly participating in the reaction, while in bifunctional effects the promoter becomes an active component either by forming new bimetallic active ensemble sites or offering new single active sites with different adsorption properties (dual adsorption). This dual adsorption can be achieved by incorporating oxophilic promoters into Pt so that the oxygenated species now adsorb preferentially on them, leaving the Pt sites free for CO adsorption and thus, facilitating CO oxidation.[18,26]

Germanium has been demonstrated to be a promising promoter for Pt. In the past, it has been used to boost the performance of Pt catalysts in a variety of reactions such as naphtha reforming[27–29] and alkane dehydrogenation.[30–36] Similarly, Pt–Ge catalysts were shown to exhibit an enhanced performance for the methanol electrooxidation.[37] In this study a reduced CO poisoning over Pt was detected, but it was proposed to arise from the surface functionalization with citric/nitric acids. Later studies showed that the adsorption properties of CO on a Pt/C surface change upon the addition of GeO_2.[38] In addition, Pt–Ge/C catalyst presents an easier CO oxidation as well as a higher electrocatalytic activity in methanol oxidation, probably due to geometric effects.[39] Ge was also tested as a promoter in Pt/SiO_2 for the CO oxidation. The experiments show that the activity and selectivity were enhanced by 2 times and 5 times, respectively due to the ability of Ge to activate O_2.[40] In this vein, a theoretical work suggested that M_2Ge_{12} compounds (M = Cr, Mn, Fe, Co and Ni) are promising catalysts for low-temperature CO oxidation, where the reaction barrier has a linear relation with the O_2 binding strength on the clusters.[41] Previously, we showed that alloying small-size Pt clusters with Ge significantly diminishes the CO poisoning, as the interaction between Pt and CO is weakened upon alloying.[42,43] Furthermore, the composition in such bimetallic catalysts might have a great influence in their physico-chemical properties.[33,43]

Building from these results, in this work, we combine first-principles calculations with microkinetic modeling to determine the role of Ge in the CO oxidation by Pt–Ge bimetallic clusters supported on MgO(100). Our aim is to verify whether the reduction of CO poisoning found thereof translates into an improvement of the catalytic activity and what Pt–Ge composition provides the best performance for this reaction. The influence of the Ge concentration on the CO and O_2 adsorption properties and the catalytic behavior is thoroughly studied. A concise mechanistic study of CO oxidation is carried out by exploring and unraveling the kinetic details of the two main pathways, *viz.*, Langmuir-Hinshelwood (LH) and Eley-Rideal (ER), along with the electronic reasons behind the observed behavior. In this way, we demonstrate that it is possible to change the bistable kinetics towards a reactive and CO poisoning-free region by adjusting the promoter content on Pt–Ge catalysts.

Computational Methods

DFT Calculations

Density functional (DFT) calculations were done using the Perdew-Burke-Ernzerhof (PBE) exchange-correlation functional[44,45] and the projector augmented wave (PAW) pseudopotentials[46] as implemented in the Vienna ab-initio simulation package (VASP).[47–50] The plane wave cutoff energy was set at 450 eV and a convergence criteria of 10^{-6} eV and 10^{-5} eV was employed for the electronic energy and the geometry relaxation, respectively. In addition, we included Grimme's semiempirical DFT-D3 corrections[51] to account

for the dispersion interactions. The Brillouin zone was sampled using a 1×1×1 Monkhorst-Pack mesh centered at the Γ point.

The Pt–Ge clusters were supported on a MgO(100) 4×4×3 slab composed of 6 layers. The bottom two layers of the support were fixed at the positions of the bulk, while the top four layers were allowed to relax. Periodic images in z direction were separated with *ca.* 15 Å of vacuum. The same ensemble of Pt_4Ge_n/MgO(100) (n = 0–4) isomers as reported in ref. [33] were used in this work. CO and O_2 molecules were adsorbed in all possible orientations on these catalysts with the global optimization toolkit PGOPT.[52] PGOPT uses the bond length distribution algorithm (BLDA) to generate a pool of initial adsorption geometries. Transition states were located with the climbing image nudged elastic band (CI-NEB) method.[53,54] It must be mentioned that in a few cases a preliminary CI-NEB run with low convergence criteria was performed followed by a tighter convergence calculation using the improved dimer method.[55,56] Due to the high computational cost, we only included the 2 uppermost MgO layers and the criteria for the forces was set to 0.05 eV Å^{-1}. The nature of the transition states was confirmed with a vibrational analysis, making sure that they only displayed a single imaginary frequency along the reaction coordinate.

The binding energy of CO and O_2 was calculated with Equation (1):

$$BE[X] = E(Pt_4Ge_n(X)/MgO) - E(Pt_4Ge_n/MgO) - E(X) \quad (1)$$

where $E(Pt_4Ge_n(X)/MgO)$ is the energy of Pt_4Ge_n cluster (n = 0–4) supported on MgO with one X molecule adsorbed, $E(Pt_4Ge_n/MgO)$ is the energy of the bare Pt_4Ge_n cluster supported on MgO and E(X) is the energy of the isolated X molecule in gas phase (X=CO, O_2). The same reference $E(O_2)$ is used for O_2 and 2×O adsorption.

Microkinetic modeling

Microkinetic modeling is a powerful technique used to analyze complex catalytic networks in terms of elementary reactions.[57,58] Herein, no assumptions are made, a priori, about the rate-determining steps or surface coverage of intermediate species. In this fashion, measured or calculated parameters such as activation and reaction free energies can be incorporated into the rate expressions. Regarding the reactor model, a continuous stirred-tank reactor (CSTR) was chosen to solve the rate equations. In this way, the time evolution of the coverages and pressures of each species can be obtained. The details of the reaction network are given in the Supporting Information. The simulations were run for at least 10^7 s to ensure convergence to a dynamic steady-state. An important point should be made here mentioning that the achieved dynamic steady-state differs significantly from the thermodynamic equilibrium as there is a continuous gas inlet and outlet which brings the system out of equilibrium in a dynamic way.[59] The total flow rate was set to 8 ml min^{-1} with different O_2: CO compositions. 100 mg of catalyst was used with a Pt loading of 0.35 wt%, based on previous experimental work.[28,60] Pt and Ge sites were treated equivalently in the spirit of the mean-field approach.

For surface reactions, the rate constants for the forward elementary reactions were determined by the transition state theory (TST) [Equation (2)]:

$$k_{f,i} = \frac{k_B T}{h} e^{\frac{-\Delta G_i^{\ddagger}}{k_B T}} \quad (2)$$

where k_B is Boltzmann's constant, h is Planck's constant and T is the temperature. $\Delta G_i^{\ddagger}$ is the Gibbs free activation energy of the i^{th} elementary reaction. The equilibrium constants K_i were calculated as follows [Equation (3)]:

$$K_i = e^{\frac{-\Delta G_i}{k_B T}} \quad (3)$$

where ΔG_i is the Gibbs free energy of the i^{th} elementary reaction. To ensure thermodynamic consistency the reverse rate constants were calculated using the corresponding forward rate constant and equilibrium constant [Equation (4)]:

$$K_i = \frac{k_{f,i}}{k_{r,i}} \quad (4)$$

The ideal gas limit was considered to compute the changes in free energy [Equation (5)]:

$$\Delta G = \Delta(E_{elec} + ZPE) - T\Delta S \quad (5)$$

where E_{elec} is the DFT computed electronic energy, ZPE is the zero-point energy and ΔS is the change in entropy. The zero-point energy was calculated from the vibrational analysis. For adsorbed species only the harmonic vibrational contribution to entropy was considered, while translational and rotational entropies were also included for gas phase species.

For non-activated unimolecular adsorption, the rate of adsorption is determined by the kinetic theory of gases [Equation (6)]:[61]

$$k_{ads} = \frac{PA}{\sqrt{2\pi m k_B T}} S \quad (6)$$

where P is the partial pressure of the adsorbate, m is the mass of the adsorbate and A is the area of the adsorption site. The adsorption site area was set equal to the area of the adjacent triangle. For O_2 chemisorption (bridge site), the area was approximated as the area of a triangle of sides Pt–Pt–Pt. For CO chemisorption (top site), the area was set to one-third of the area for O_2. S is the sticking coefficient and was set to 1 for all species, based on their favorable adsorption energies.

Results and Discussion

CO and O_2 Adsorption on Pt_4Ge_n/MgO(100) (n = 0–4)

Before moving to the discussion of the CO reaction mechanisms we first study the adsorption of the reactants, *viz.*, CO and O_2, on Pt_4Ge_n/MgO with n = 0–4. These surface-mounted nano-clusters have been recently characterized and are predicted to be synthetically accessible under Ge-rich conditions.[33] For each composition, various conformers would coexist since they are energetically competitive, except for Pt_4Ge in which a single isomer, the global minimum (GM), dominates the population. Note that, while all the bimetallic clusters have a closed-shell electronic structure, Pt_4/MgO possesses unpaired electrons in most cases.[33] Because isomers can exhibit different reactivity, CO and O_2 were adsorbed on the most populated conformers of each Pt_4Ge_n composition. The resulting most stable adsorption geometries along with the CO and O_2 binding energies (*BE*), Boltzmann populations of each structure at 500 K, and Bader effective charges are summarized in Figure 1. The first

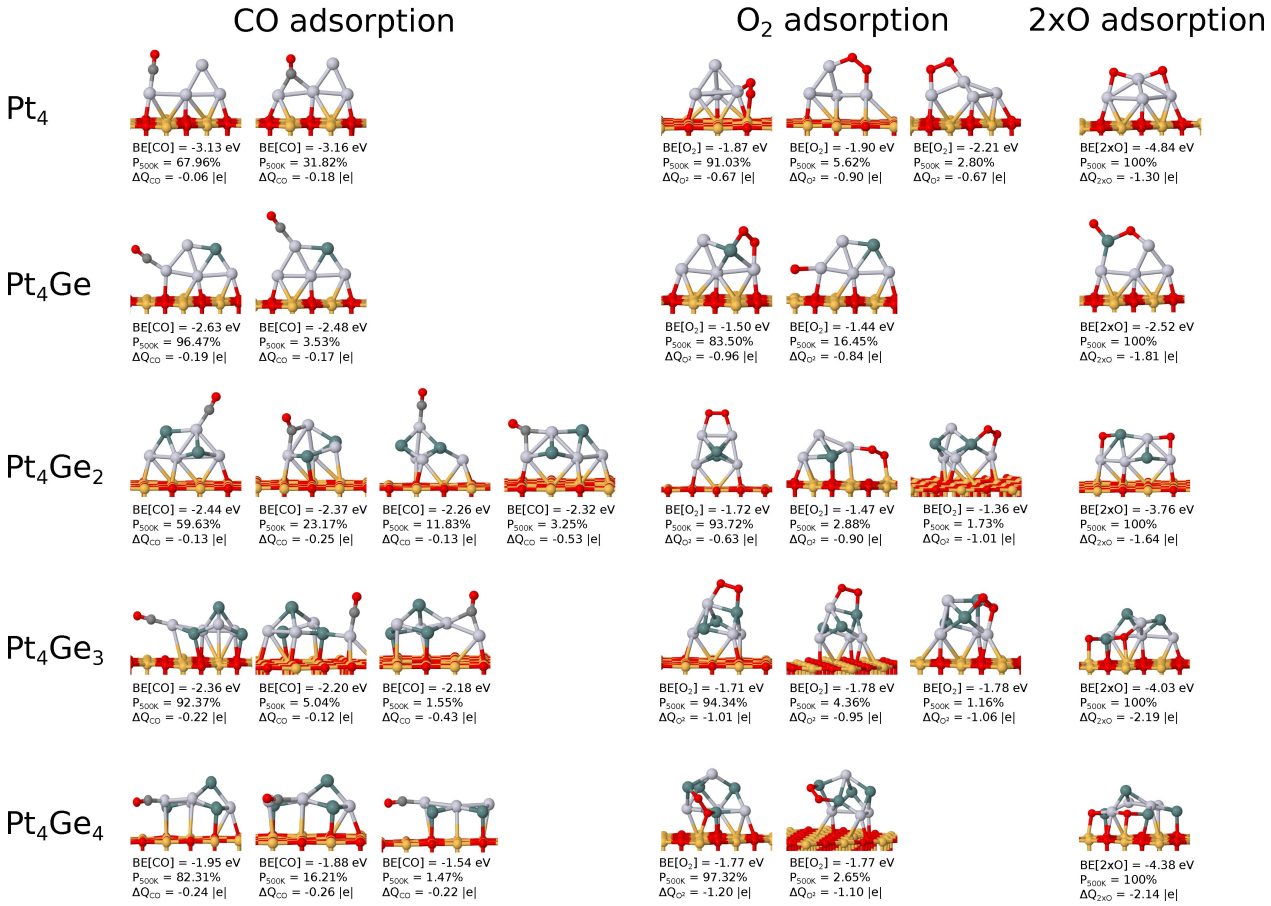

Figure 1. Most stable CO, O_2 and 2×O adsorption geometries on Pt_4Ge_n/MgO(100) clusters along with the ligand binding energies (*BE*s) in units of eV, Boltzmann populations at 500 K (P_{500K}) and charge transfer to ligand (ΔQ) in values of $|e|$. Only isomers with $P_{500K} > 1.00\%$ are shown. Pt, Ge, Mg, O and C are depicted in gray, dark green, orange, red and dark gray, respectively.

thing to note is that after adsorption the size of the ensemble and the relative stability of the isomers changes, showing the dynamic effect of adsorption.[15] CO adsorption has a profound effect on the cluster population. For instance, in Pt_4Ge_3, isomer IV in ref [33] (population at 500 K of 8.3 %) becomes predominant upon CO adsorption, while the most stable bare clusters become negligible. In general, CO prefers to adsorb on Pt through the C end in an atop configuration (∠Pt–C–O 180°), with a few exceptions, where it binds in a bridge fashion. CO adsorption has little impact on the cluster geometry, and CO is never found adsorbed on Ge which indicates the much higher preference towards Pt. O_2 is found to adsorb either dissociatively (2×O*) or non-dissociatively (O_2*). Contrary to CO, oxygen can bind to both Pt and Ge, the most common active site being a bimetallic Pt–Ge ensemble. In the dissociative adsorption atomic O binds in a M–O–M bridge configuration, while in the non-dissociative adsorption it usually adopts a M–O–O–M two-member bridge site. It should be noted that in many isomers O* adsorbs at the cluster-support interface bonded to a Mg atom, which is in stark contrast to CO. Moreover, a significant distortion is observed upon adsorption due to the oxophilicity of Ge. In some adducts (*e.g.*, Pt_4Ge2O isomer I) O* opens the Pt–Ge polar bonds deforming the structure. This effect may become more significant at strong oxidizing conditions.

The Sabatier principle states that the binding strength between reactants and catalysts should not be very strong to avoid overbinding and poisoning effects, nor very weak to give enough time for diffusion and collision. In addition, the products should interact weakly with the surface to guarantee a facile desorption. In Figure 1, pure Pt_4CO presents the largest CO binding energy (isomer I, *BE*[CO] = −3.13 eV), suggestive of a tendency to undergo CO poisoning. Nonetheless, adding a single Ge atom in Pt_4GeCO, the *BE*[CO] is reduced to −2.63 eV; and as the Ge concentration increases a gradual drop in the *BE*[CO] is observed. This trend is in line with previous observations in gas-phase and graphene-supported Pt–Ge nanoclusters.[42,43] The bonding between Pt and CO can be understood in terms of the Blyholder model.[62] Briefly, it describes the interaction with an electron transfer from the 5σ of CO to the empty Pt d orbitals (donation step), and an electron transfer from the Pt d orbitals to the empty 2π* of CO (back-donation step). According to the Bader analysis (Figure 1) and projected density of states (PDOS, Figure S3), there is a net charge transfer from the cluster to CO 2π*. As a result, the C–O

bond is weakened and elongated slightly from 1.14 Å in gas-phase to ~1.17 Å.

As stated above, for O_2 both the molecular and dissociative adsorptions are competitive. Comparing the binding energies to oxygen it is evident that the latter is more stable than the former; as explained in the next section, O_2 dissociation is an exothermic process. Overall CO is more strongly adsorbed than molecular oxygen. The same is true for atomic oxygen in monometallic and Pt $_4$Ge clusters. However, as the Ge concentration increases, the adsorption of 2×O* becomes stronger than that of CO* by more than 2 eV in Pt_4Ge_3 and Pt_4Ge_4, meaning that O* may become the predominant species on the catalyst surface. Regardless of the adsorption mode, O atoms carry a negative charge owing to an electron transfer from the cluster to the empty 2π* orbitals. As expected, dissociated O* has a significantly larger charge than molecular O_2* since a single atom is interacting with two Pt or Ge atoms. Depending on the degree of activation (O–O elongation) molecular O_2* can change its electronic state. In gas-phase the diatomic distance is 1.21 Å (bond order = 2). Upon adsorption, the internal bond weakens (bond order reduction) and elongates. If one electron is transferred to oxygen, the superoxo (O_2^-) state is obtained with a O–O bond distance of ~1.33 Å (bond order ~1.5). O_2* can still accept another electron and achieve the peroxo (O_2^{2-}) state with a O–O bond distance of ~1.47 Å (bond order ~1.0). Our calculations suggest a large oxygen activation for the Pt–Ge nanoclusters. The internal bond is increased up to 1.47–1.50 Å in the bidentate bridge configuration, indicating the presence of a peroxo state; while in the top configuration it is only activated until the superoxo state with a bond length of 1.37 Å. We believe that such a high activation translates into low oxygen dissociation barriers.

O_2 Dissociation on Pt_4Ge_n/MgO(100) (n = 0–4)

To investigate the O_2 molecular and dissociative adsorption mechanisms, we have computed the O_2 dissociation barriers The energy profiles for the different Pt_4Ge_n clusters are collected in Figure 2. Here, we only show the results for the pathways with the most stable Pt_4Ge_n2O final state (FS) adducts for each cluster; the rest of the isomers are depicted in Figures S4–S7 of the SI.

After O_2 chemisorption, the cluster activates the O–O bond by transferring electrons to the antibonding 2π* orbitals. For the bridge adsorption mode O_2 is activated in the peroxo state where the IS structure is close to the transition state (TS). The cluster continues to stretch the bond until finally the O–O scission is achieved. In all cases the O–O bond is already cleaved in the TS, even for the atop adsorption (see Figure S4). Our calculations reveal that the O–O bond expands from ~1.47 Å to a value in the range of 1.90–2.15 Å in the TS. Here the charges of the O atoms are maximal; each atom carries 0.6–0.8|e| comparing to ~0.4 |e| in the IS. The values of these charges are similar for adsorption on Pt–Pt and Pt–Ge of M–O–O–M bridge sites. For the numerical values of the oxygen Bader charges and O–O distances the reader is referred to Table S1. Afterwards, the O atoms separate and occupy a bridge site in the vicinity. This process is found to be exothermic, the greatest energy release occurring when the strong Ge–O bonds distort the cluster structure (*e.g.*, Pt_4Ge_4 isomer II, Figure S7). Overall, the activation barriers are small and most cases lie in the range of 0.4–0.6 eV, although there are some exceptions where the barrier increases to 0.75 eV, as for the Pt_4Ge_3 isomer I (see Figure S6). Our results indicate that at room temperature most of the adsorbed oxygen will be in the form of atomic O*.

CO Oxidation on Pt_4Ge_n/MgO(100) (n = 0–4)

Here, we characterize the potential energy surface of CO oxidation on Pt_4Ge_n clusters (n = 0–4) supported on MgO(100). On Pt-based catalysts, CO oxidation usually proceeds via the bimolecular LH or ER mechanisms. In LH prior to the reaction both CO and O_2 are adsorbed on the surface, that is, co-adsorption of the reactants is required. Then the reactants diffuse to adjacent sites and react with each other to form CO_2, which is released to the environment. Besides, the ER mechanism only involves O_2 adsorption followed by a CO attack in the gas-hase. As has been confirmed in the previous section, all clusters present small oxygen dissociation barriers. Hence, CO will be able to react not only with O_2* but also with O*; in other words, both O_2 and O are available as oxygen sources. We must highlight that all the possible reaction mechanisms were characterized by considering two different structures for each Pt_4Ge_n/MgO, the isomers with the most stable IS and FS in the O_2 dissociation shown in Figures 2 and S4–S7. $Pt_4Ge_nO_2$ was used to study the routes involving CO + O_2, while Pt_4Ge_n2O was employed for the CO + 2×O paths. Since the starting point involves two oxygen atoms in either case, two steps will be needed to complete the catalytic cycle, *i.e.*, the formation of two CO_2 molecules.

Eley-Rideal mechanism

The ER mechanism takes place when CO in the gas-phase attacks O_2* or predissociated O* on the surface. Given the small size of the nanoclusters explored in this work, the variety of co-adsorption configurations is limited, and hence the ER mechanism may actually be a competitive mechanism within this size regime. Figure 3 shows the reaction pathways for both CO(g) + O_2* and CO(g) + 2×O* for all Pt_4Ge_n considered in this section. For the sake of clarity, we only show the results for the first CO_2 formation in both routes; the second CO_2 formation is depicted in Figure S8.

As depicted in Figure 3, CO(g) attack to O_2* always occurs from the C end. As CO approaches the molecules, the O–O bond starts activating until the TS is reached. It should be remarked that the TS is effectively achieved only under certain angles of attack (∠O–C–O* between 120° and 125°). In the TS, CO(g) is found at a distance of ~1.70 Å from O_2. The CO internal bond is almost unchanged while O–O is activated to ~1.68 Å. After the energy barrier is successfully overcome, CO_2 is directly

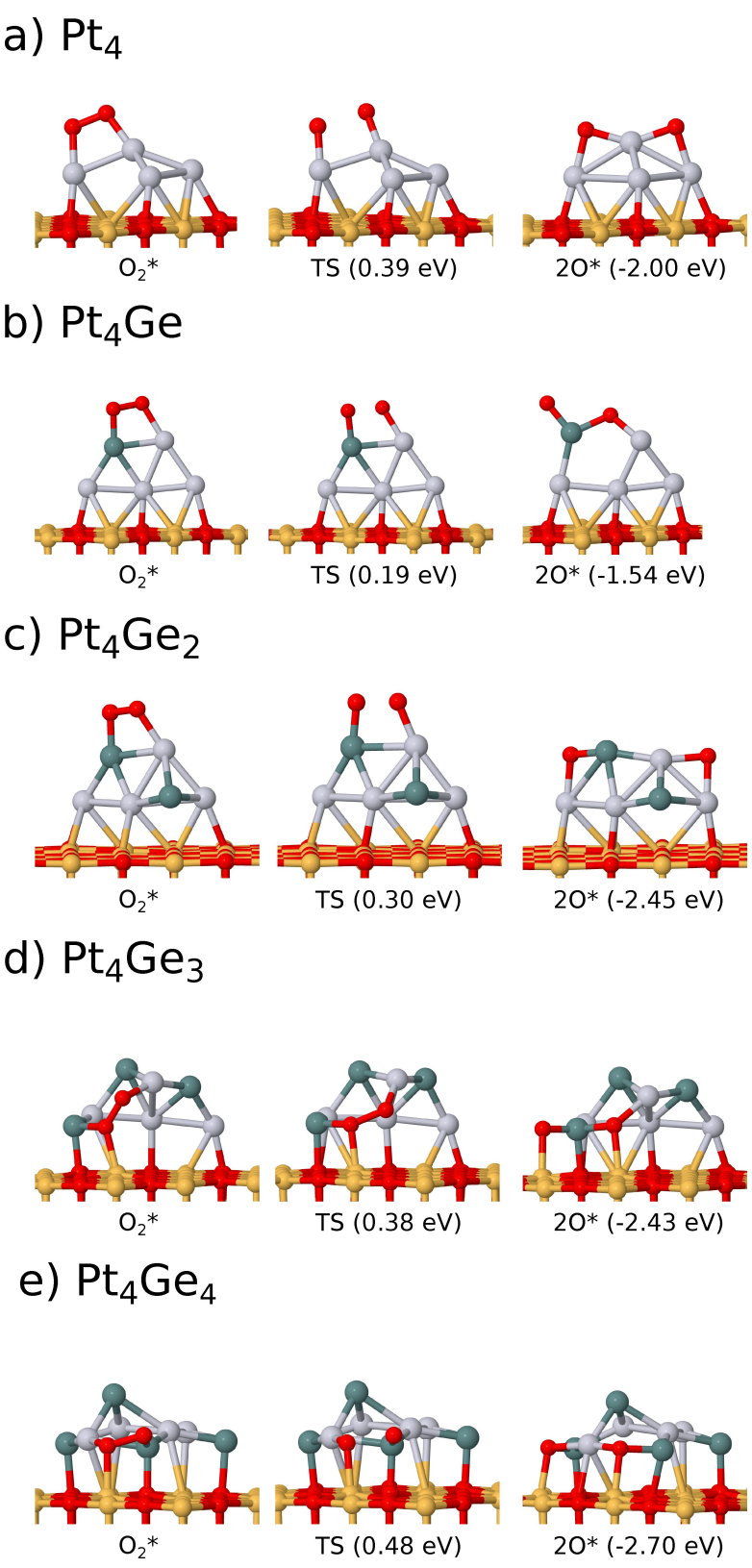

Figure 2. Initial state (IS), transition state (TS) and final state (FS) geometries for the O_2 dissociation pathway on the Pt_4Ge_n/MgO(100) isomers with the most stable final state (FS). Activation and reaction energies (in eV) are given relative to the corresponding IS. Pt, Ge, Mg, O and C are depicted in gray, dark green, orange, red and dark gray, respectively.

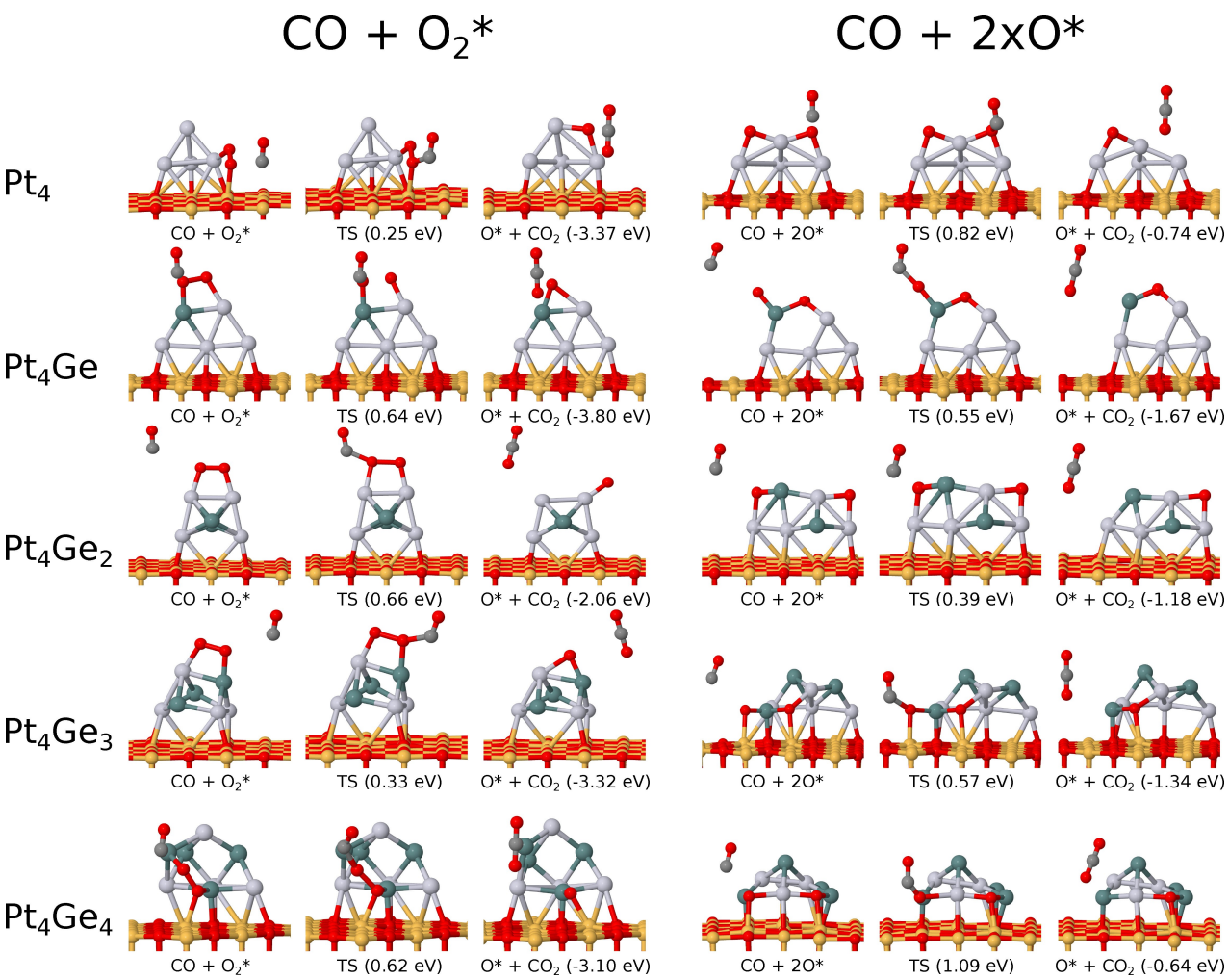

Figure 3. Most stable reaction pathways for the Eley-Rideal (ER) mechanism for both molecular and dissociated oxygen reactions on Pt_4Ge_n/MgO(100). Initial state (IS), transition state (TS) and final state (FS) geometries are shown together with the relative activation and reaction energies (in eV). Only the first step is given. Pt, Ge, Mg, O and C are depicted in gray, dark green, orange, red and dark gray, respectively.

ejected from the surface without the formation of an intermediate state (IM). The corresponding energy barriers for this route are rather small; Pt_4 has a barrier of 0.25 eV, whereas in the nanoalloys it lies in the range of 0.30–0.60 eV. In contrast, in the most likely route, the CO(g) + 2×O* route (Figure 3), the barriers on Pt_4 increase up to 0.80 eV. Pt_4Ge (second step) and Pt_4Ge_4 (first step) also show high barriers of 1.0 eV, whereas in the clusters with medium Ge content they remain below 0.60 eV. All steps are found to be exothermic. These results suggest that Pt_4Ge_2 and Pt_4Ge_3 are the most active compositions. Nonetheless, as long as there is predissociated O*, *i.e.*, CO poisoning is avoided, the reaction will move forward in all cases and thus, the ER channel will proceed similarly regardless of the Pt–Ge composition.

Langmuir-Hinshelwood mechanism

In Figure 4 we display the reaction pathways through the first step of the LH channel for CO oxidation by both molecular and atomic oxygen on Pt_4Ge_n clusters; the second step is depicted in Figure S9.

To search for the most suitable starting point a screening of the most stable co-adsorption complexes was done by adsorbing CO with multiple orientations on adjacent sites to O_2* or O* in $Pt_4Ge_nO_2$ and Pt_4Ge_n2O. We begin with the CO* + O_2* reaction (Figure 4). As the reactants approach each other the O–O bond is elongated and the reaction proceeds via the first TS to an intermediate (IM). It should be mentioned that in many cases[63] this first step involves the formation of a OCOO* species in the IM. However, our calculations for Pt–Ge reveal that the cleavage of O–O and formation of C–O occurs simultaneously in the first step, so CO_2* is already formed in the IM. Apart from Pt_4Ge, oxygen is already dissociated in the TS. The charge of the reacting O increases up to ~1.0 |e|. In the IM complex CO_2 is usually bonded from the C atom to Pt with a Pt–C distance of ~2.05 Å and has an internal angle of ~130°. When the reaction occurs close to the interface, CO_2 also binds to a substrate Mg atom via one of the oxygens. Subsequently, there is a barrierless

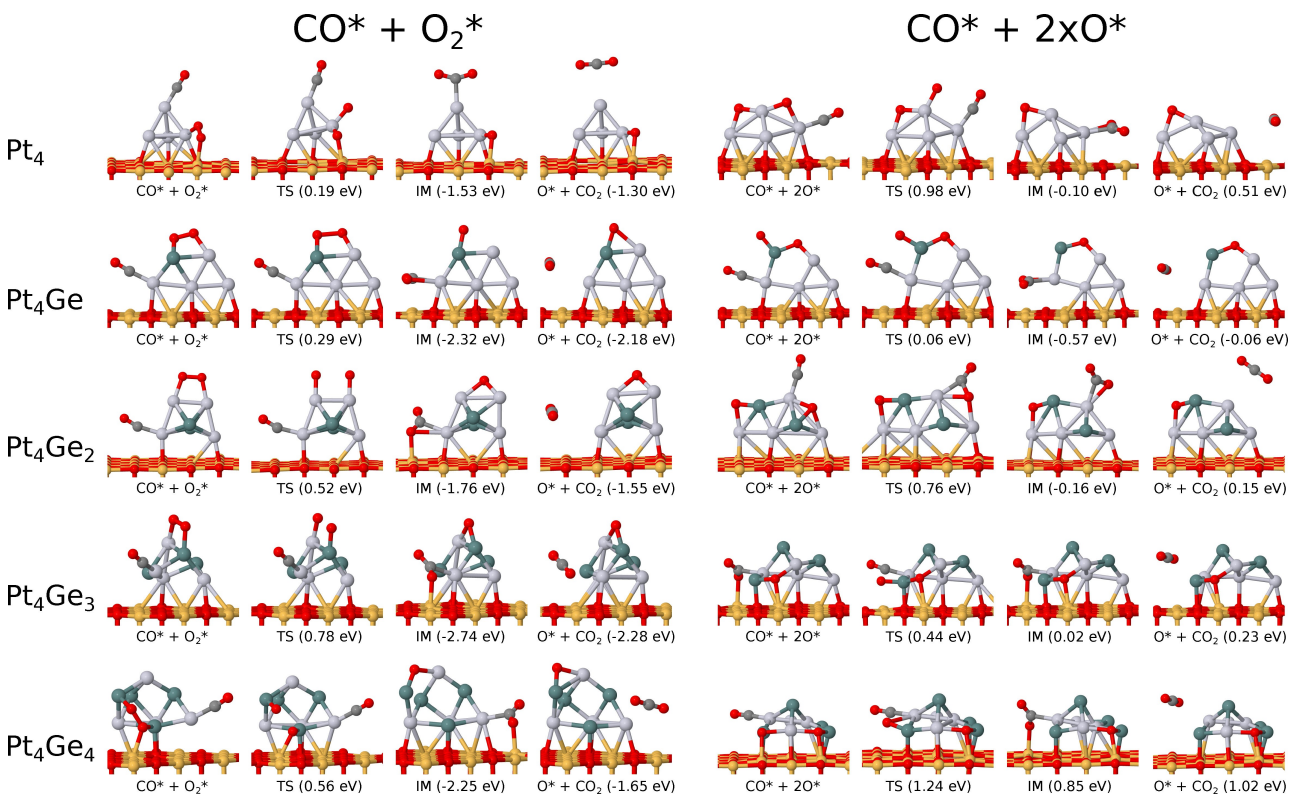

Figure 4. Most stable reaction pathways for the Langmuir-Hinshelwood (LH) mechanism for both molecular and dissociated oxygen reactions on Pt_4Ge_n/MgO(100). Initial state (IS), transition state (TS), intermediate state (IM) and final state (FS) geometries are shown together with the relative activation and reaction energies (in eV). Only the first step is given. Pt, Ge, Mg, O and C are depicted in gray, dark green, orange, red and dark gray, respectively.

release of the formed CO_2 molecule to the environment, leaving an O* on the surface to further oxidize another CO molecule.

Pure Pt_4 presents small barriers for the first (0.19 eV) as well as the second step (0.50 eV). Regarding the bimetallic counterparts, the first step for Pt_4Ge and Pt_4Ge_2 are also rather small (0.29 and 0.52 eV), whereas the second barrier becomes significantly large (> 1.5 eV), while O* has to migrate from one very stable bridge position to the adjacent one. In Pt_4Ge_3 the first CO_2 formation shows a barrier of 0.78 eV, while in Pt_4Ge_4 both barriers are around 0.55 eV. The first step is always more exothermic than the second as the O–O scission releases extra energy. CO_2 desorption is found to be endothermic with a *BE* of around 0.10 eV and 0.30 eV in the first and second steps, respectively.

The most likely scenario, however, is the one where CO* reacts with predissociated O* (CO* + 2×O*), as shown in Figure 4. A detailed inspection reveals that in the TS of this channel CO* and O* are closer than in CO* + O_2*. The reactants are bonded on top of neighbouring atoms and oriented parallel to each other, forming a cyclic Pt–C–O–Pt(Ge) structure. The length of the "to be formed" C–O bond lies between 2.75 and 2.90 Å. Such TS structure has also been observed previously in the CO oxidation by small Pd clusters.[64] Contrary to the previous pathway, Pt_4 has to overcome now larger barriers of ~1.0 eV in both steps. Surprisingly, on Pt_4Ge the first step proceeds almost barrierless, although the second oxidation is highly unfavorable. On the contrary, Pt_4Ge_2 and Pt_4Ge_3 show the best balance between the two steps with low barriers. Moreover, in this route the first IM formation is significantly less exothermic since the reaction starts from a very stable complex. Except for Pt_4Ge_4 (0.85 eV), the first IM formation is still slightly exothermic, while the second step is predicted to be exothermic only on Pt_4Ge_3 and Pt_4Ge_4 (see Figure S9). Another observation of critical importance is the fact that CO_2 removal becomes highly endothermic in Pt_4, especially in the second step, as opposed to the alloys. This suggests a tendency to get poisoned by CO_2.

It is extremely important to consider the statistical weights of each reaction channel. Indeed, the most likely reaction mechanism for LH will be connected to atomic oxygen. In this case bimetallic clusters present lower energy barriers as compared to pure Pt, as well as the inhibition of the CO and CO_2 poisoning effects.

For the sake of comparison, the complete potential energy diagram of the LH mechanism with predissociated oxygen on all the Pt_4Ge_n nanoclusters is illustrated in Figure 5 (the reader is referred to Figure S10 for the results of the other cases). It can be observed that the LH mechanism lies lower in energy than ER since it includes the adsorption of both O_2 and CO, while ER is missing the adsorption of CO. In the ER mechanism for both CO(g) + O_2* and CO(g) + 2×O* (Figure S10), all steps are exothermic (downhill) for all clusters, the CO_2 release being the most stable state. Consequently, this state will act as a thermodynamic sink shifting the reaction towards CO_2 forma-

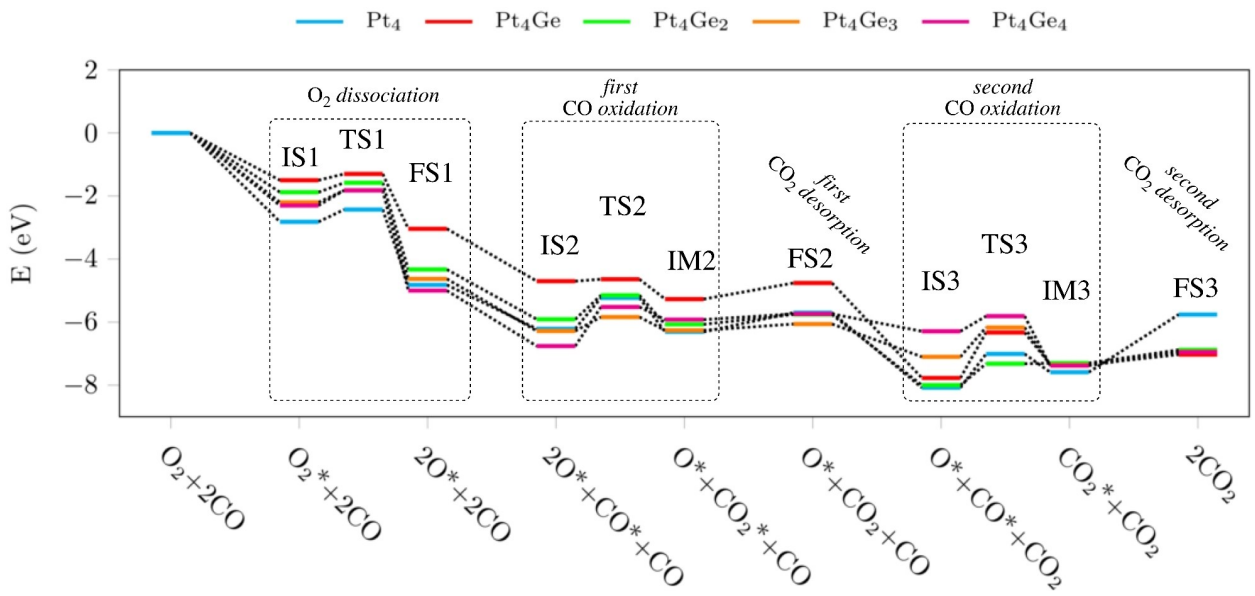

Figure 5. Potential energy diagram of the most stable CO*+2×O* routes (LH mechanism) on Pt_4Ge_n/MgO(100). Energies (in eV) are given relative to the clean Pt_4Ge_n/MgO(100) surface.

tion, regardless of the Ge concentration. Notwithstanding, as shown in Figure 5, in the LH mechanisms O*+CO* (IS3, O*+CO*) becomes the most stable state for Pt_4, Pt_4Ge and Pt_4Ge_2 due to the endothermic nature of the last two steps (second oxidation+desorption). This indicates that IS3 will act as a drain and shift the reaction towards CO*+O* formation. In this state O* could still react with CO in gas-phase via ER mechanism, but part of the surface will be poisoned by CO. The case of Pt_4 is more dramatic since CO_2 desorption is highly endothermic, which means that part of the formed CO_2 will remain on the surface, *i.e.*, Pt_4 will be poisoned by CO_2 as well as CO.

Contrary to pure Pt, the formation of the second CO_2* (IM3) becomes the lowest stationary point when increasing the Ge content, *i.e.*, in Pt_4Ge_3 and Pt_4Ge_4. Because CO_2 desorption is slightly endothermic in both cases, CO_2 will easily detach from the cluster. On Pt_4Ge_3 the oxidation steps are somewhat reversible, while on Pt_4Ge_4 the first step is very endothermic. From these observations it can be concluded that in either case the surface will be covered by CO*, O* and CO_2*, but in Pt_4Ge_3 once CO_2(g) is formed, the reaction will evolve more easily towards the final product. Furthermore, these two clusters present a higher *BE* for O_2 than CO, so O* may become the predominant species together with CO_2*, limiting CO poisoning. The O* in excess should not be considered detrimental since it can still react with CO(g) via the ER channel. In reality, CO is being consumed simultaneously in each one of these routes; in other words, the different pathways are not independent of each other and the reaction should be thought of as a dynamic phenomenon where the coverage of the intermediates obtained through one route may affect the efficiency of the other. Such a relationship cannot be captured with the results obtained so far. In this respect, microkinetic modeling can be a very useful tool to help elucidate the time evolution of complex reaction networks.

Microkinetic simulations

To shed light on the effect of the alloy concentration over the time evolution of CO_2 production, the DFT calculations were complemented with an 8–step microkinetic model, following the approach of previous work.[65,66] Microkinetic modeling allows us to make a more direct comparison between DFT calculations and experimental variables such as partial pressures and temperatures. Importantly, the coverage effects are also considered, offering a thorough assessment of the catalyst poisoning tendency. In the simulations reported herein, the temperature was varied from 100 to 500 K and the O_2:CO ratio of the feed was altered to simulate different environments (*viz.*, $P_{O2}=0.5$ bar, $P_{CO}=0.5$ bar; $P_{O2}=0.5$ bar, $P_{CO}=0.05$ bar; $P_{O2}=0.05$ bar, $P_{CO}=0.5$ bar). It should be stressed that no a priori assumptions were made about the rate-determining step or steady-state surface coverages. The elementary steps and reactor model are described in greater detail in the SI.

In Figure 6 we compare the steady-state coverages and the CO_2 turnover frequency (TOF_{CO2}) as a function of temperature and CO and O_2 partial pressures of Pt_4 (pure Pt) with the best alloy candidate, *i.e.*, Pt_4Ge_3; the rest are shown in Figure S12, along with the discussion. A quick glance reveals that Pt_4 exhibits the well-reported bistable kinetics in agreement with previous studies.[6,67,68] Different regimes of slow (severe CO poisoning; Figure 6a, right) and fast (CO poisoning-free; Figure 6a, left) kinetics can be distinguished based on the surface coverages. High O_2 pressures are the best conditions to avoid CO poisoning and increase the CO_2 formation rate. At equal CO and O_2 pressures (Figure 6a, middle), O* (θ_O ~0.5 ML) and CO_2* (θ_{CO2} ~0.4 ML) become the main species on the surface in the range of 100–200 K. Interestingly, despite using a feed with a CO:O_2 1:1 composition, the CO coverage only amounts to 0.1 ML. In this temperature regime, Pt_4 is more reactive in the

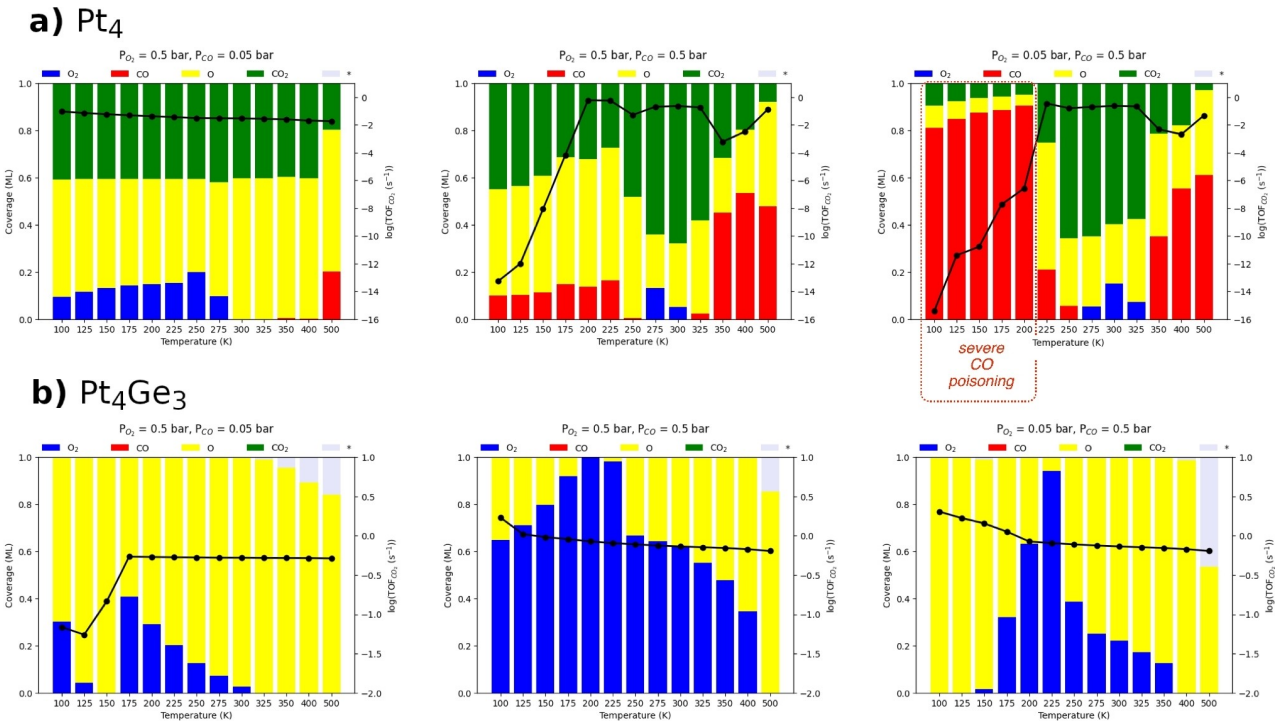

Figure 6. Microkinetic analysis of CO oxidation for a) Pt_4 and b) Pt_4Ge_3 clusters supported on MgO(100). Steady-state coverages and CO_2 turnover frequencies (TOF_{CO2}) as a function of temperature with different feed compositions: $P_{O2}=0.5$ bar, $P_{CO}=0.05$ bar (left figure); $P_{O2}=0.5$ bar, $P_{CO}=0.5$ bar (middle figure); $P_{O2}=0.05$ bar, $P_{CO}=0.5$ bar (right figure).

$CO^*+O_2^*$ route than in the CO^*+O^* one (see Table S3), making the former the predominant path for CO_2 production. The high endothermicity of CO_2 desorption makes CO_2^* block an important portion of the free active sites. In addition, the O* produced via $CO^*+O_2^*$, remains mostly unreacted owing to the high energy barrier in the CO^*+O^* route (see Table S3), which becomes reflected in the low TOF_{CO2} values. At intermediate temperatures (200–325 K) CO_2^* becomes the predominant species which may be ascribed to an increment in the CO_2 desorption free energy. The TOF_{CO2} also increases and remains constant at a fairly moderate level (TOF_{CO2}~10^{-1} s^{-1}). It should be noted that O* is constantly reacting with CO in gas-phase via ER mechanism. The empty sites left will either become covered with O* again or CO* and CO_2^* (the latter being more likely). Then, from 350 K upwards, a change of mechanism occurs and CO^*+O^* becomes the main route (see Table S3). The barriers for O_2 dissociation and CO^*+O^* reaction become lower than the $CO^*+O_2^*$ ones. Yet, the difference in binding free energies (*BG*s) between CO and O_2 becomes more important, and therefore CO poisoning also becomes more pronounced, slowing down the reaction rate.

At high O_2 pressures (Figure 6a, left) a transition can be observed to the CO poisoning-free regime. Higher O_2 pressures seem to be beneficial, regardless of the temperature, as expected. O_2 adsorption becomes more favorable than CO (see Table S3), which then converts to O* via O_2 dissociation and $CO^*+O_2^*$. From 100 K to 275 K the surface composition is 0.4 ML CO_2^*, ~0.5 ML O* and ~0.1 ML O_2^*. At higher temperature, O_2 dissociation becomes more favorable and O* coverage increases at the cost of O_2^* sites. The presence of CO_2^* indicates that the LH channel is not hindered by CO poisoning. However, CO_2^* limits the availability of active sites for LH and ER pathways, so the efficiency of CO_2 production is compromised. The TOF_{CO2} decreases linearly with temperature from 10^{-1} to 10^{-2} s^{-1}. We anticipate that CO_2 poisoning can cause a drop in the TOF_{CO2} by two orders of magnitude, although the effect is milder than for CO poisoning.

A CO-rich feed (Figure 6, right) has an extremely detrimental effect on the performance of the monometallic cluster at low temperatures; Pt_4 becomes almost completely poisoned by CO (θ_{CO} ~0.8 ML). In this regime there is a scarcity of O_2^* and O* sites for LH and ER paths and thus the oxidation rate decreases drastically. This behavior can be understood in terms of DFT binding free energies that show the strong adsorption of CO on pure Pt clusters. The TOF_{CO2} increases with temperature until it is stabilized in the 225–325 K window. CO* nearly disappears but CO_2^* coverage becomes more pronounced (θ_{CO2} ~0.6 ML). Nonetheless, there is still a fraction of O* and O_2^* which can oxidize CO at rates similar to $P_{O2}>P_{CO}$. As the temperature increases, CO* coverage starts increasing at the expense of CO_2^* and the TOF_{CO2} is slightly reduced.

We must emphasize that CO and CO_2 poisoning are completely suppressed in Pt_4Ge_3 under the conditions studied in this work (see Figure 6b). CO coverage is negligible even at $P_{CO}>P_{O2}$. Our results indicate that the bistable kinetics of CO oxidation disappears; a single regime of fast CO oxidation rate is obtained by controlling the promoter concentration. The three different pressure conditions show very similar behaviour.

O_2* and O* are always the only species found at steady-state. The O_2* coverage changes in a pyramid-like fashion, showing the highest value at intermediate temperatures. At $P_{O2} = P_{CO}$, O_2* remains the main dominant species until 350 K, whereas at $P_{O2} > P_{CO}$, O* coverage becomes larger in the whole temperature range due to greater availability for O_2 dissociation sites. We highlight that the Pt–Ge nanoalloy starts to show very similar *BG*s for CO and O_2 at this precise Ge concentration. Thus, both reactants will adsorb with similar probabilities, and according to the Sabatier principle, the conditions for CO oxidation will be optimal. The importance of the magnitude of the binding energies on the overall performance of the reaction kinetics has been underlined previously.[69] In addition, Pt_4Ge_3 shows much faster kinetics for the CO* + O* than CO* + O_2* step (see Table S3 for the corresponding reaction rates). This means that at initial times the TOF_{CO2} will be small as there will only be present CO* and O_2*. But once O_2 starts dissociating, CO* will react immediately with the newly formed O* to give CO_2. O_2* accumulation is not problematic since it can dissociate to O* or react with CO(g) via ER. It is also important to mention that CO_2 desorption becomes spontaneous with increasing temperature, which prevents CO_2 poisoning.

Except at $P_{O2} > P_{CO}$, the TOF_{CO2} is higher at low temperatures and slightly decreases monotonically with temperature, but always maintains at high value. Interestingly, the highest TOF_{CO2} is obtained at 100 K for $P_{O2} = P_{CO}$ and $P_{CO} > P_{O2}$, which is at least one order of magnitude higher as compared to other compositions. Part of these results may be found somewhat counterintuitive. However, we believe that this behaviour might be the result of the interplay between two effects, *i.e.*, entropic and the dynamic nature of the steady-state. First, the DFT results reflect that the Gibbs free energies of the reactions and barriers have a substantial dependence with temperature (see for instance Figure S11). This alters the viability of the different reaction channels (e.g., CO* + O* *vs* CO* + O_2*) at different temperatures, and thus, yields different steady-state coverages and TOFs. Second, it should be kept in mind that in CSTR conditions the system is not at thermodynamic steady-state (equilibrium) but at a dynamic steady-state, which depends on the gas in/out flow. Namely, the constant flow of gas species also affects the surface composition and can in turn shift the elementary reactions at either direction with different strength. One should be cautious to rely solely on equilibrium data to rationalize the behaviour of systems out of thermodynamic equilibrium. The changes occur so that O_2* is formed at the expense of O*, showing a pyramid-like behaviour. Unfortunately, quantifying this hypothesis is out of the scope of this work. Preliminary steps were done by performing a degree of rate control (DRC) analysis, but unfortunately we faced numerical instabilities with the evaluation of numerical derivatives. Finite difference method has already been reported problematic previously,[70] especially in transient kinetics where the magnitude of the finite-size perturbation can affect the convergence of the dynamic steady-state.[71]

Besides, it is important to point out that Pt_4Ge_3 will also get poisoned eventually at higher CO pressures. The bistable kinetics is a property inherent to CO oxidation. Ge alloying acts by increasing the boundaries of the fast kinetic regime to harsher conditions in the P–T phase diagram. The CO-poisoning region does not disappear, although it will occupy a much smaller portion of the phase diagram compared with pure Pt_4.

Regarding the role of Ge, DFT results suggest that on the one hand, Ge induces ligand effects (electronic effects) on Pt and reduces the affinity to CO, avoiding the overbinding of CO over O_2. Similar ligand effects were also observed by Molina *et al.* for Nb and Mo doping.[72] The advantageous mixing between both elements guarantees that Ge hybridizes with most Pt sites in the nanoalloy. On the other hand, our theoretical findings suggest that Pt–Ge also acts as a bifunctional catalyst. The addition of Ge into the catalyst creates new active sites for a more efficient oxygen adsorption. The nanoalloys show a dual adsorption behavior where CO is preferentially adsorbed on Pt and O_2 on Ge avoiding the competition for the active sites. Such behavior is in line with other oxophilic promoters such as Ru, Mo or Sn.[18,26] Although in many instances Pt–Ge ensembles are needed for O_2* and O* bridge adsorption, the ligand effects provide a similar adsorption strength to CO. Again, the high mixing guarantees that CO* and O_2* (or O*) sites are in proximity for a facile diffusion and reaction, maximizing the bifunctional effect. Importantly, the ligand and bifunctional effects depend on Ge content, *i.e.*, Ge alloying offers a new degree of freedom to control the catalytic properties of bimetallic catalysts. Apparently, this concentration dependence is very reaction-specific. Our results suggest that Pt_4Ge_3 composition has the most adequate reactivity for CO oxidation, in contrast to dehydrogenation reactions where Pt_4Ge outperforms Pt_4Ge_3.[33]

The microkinetic simulations further confirm that Ge alloying alters the CO oxidation bistable kinetics. Ge leads to a CO poisoning-free regime and fast CO_2 production prevails, at least within the pressure ranges studied in this work. Besides, the microkinetic simulations reveal that in this regime the Pt–Ge clusters may exhibit a high oxidation state (high O* coverage). Although our microkinetic model does not distinguish between Pt and Ge sites, the information about the binding energies is included; and thus, this high oxidation state may be indicative of a bifunctional mechanism. By virtue of these findings and previous work on bigger NPs,[40] we speculate that part of the subnano catalyst may remain reduced to the metallic state with Pt–Ge alloy formation, and part may be oxidized to GeO_x. Therefore, now there is available an independent oxygen reservoir resistant to CO poisoning, *i.e.*, GeO_x, which can react with CO on Pt metallic sites.

Conclusions

We have studied the effect of the composition on the CO oxidation reaction catalyzed by Pt_4Ge_n clusters (n = 0–4) supported on MgO(100) using a combination of DFT and microkinetic simulations. To characterize the most stable CO and O_2 adsorption configurations, a global minima search was carried out on the thermally populated isomers of each cluster composition. The DFT results reveal that CO binding energy

weakens with the Ge content owing to ligand (electronic) effects induced on Pt upon Ge alloying. Bond-length and PDOS analysis indicate that O_2 is readily activated up to the peroxo state and dissociates to atomic oxygen with low barriers and significant release of energy in all the Pt_4Ge_n clusters.

A systematic study of CO oxidation is performed by considering the LH and ER mechanisms initiated by both molecular and atomic oxygen. In the ER mechanism pure and alloyed clusters present similar barriers and the whole process is downhill. Nonetheless, a pronounced dependence on the Ge concentration is found for the LH pathway, which is the most likely reaction channel. For Pt_4, the barriers for the $CO^* + 2{\times}O^*$ are *ca.* 1 eV. In addition, pure Pt is prone to become poisoned by CO and CO_2. On the contrary, the poisoning effects are overcome on Pt–Ge. Pt_4Ge, Pt_4Ge_2 and Pt_4Ge_4 present acceptable reaction barriers except one of the steps in the $CO^* + 2{\times}O^*$ route which is blocked with relatively high activation and reaction energies. For Pt_4Ge_3, all the reaction barriers are attainable (< 1 eV).

The microkinetic simulations hint to a reduced CO and CO_2 poisoning dependence with increased Ge concentration. Pt_4 shows a bistable-like CO oxidation kinetics, in agreement with the literature. At low temperatures and/or high CO pressures it suffers from CO poisoning and CO_2 production drops drastically. On top of this, regardless of partial pressures, there is a constant CO_2 poisoning which also diminishes the TOF_{CO2}. Nevertheless, as the Ge concentration increases CO and CO_2 poisoning subside, until in Pt_4Ge_3 the kinetic regime of severe CO poisoning is removed. A 4:3 Pt to Ge ratio changes the bistable kinetics of pure Pt and instead, a regime of fast CO_2 formation is obtained for all temperatures and pressures considered. CO_2 poisoning does not change in the same way with the Ge content as Pt_4Ge_4 again shows some CO_2 poisoning. Thus, Pt_4Ge_3 appears to be the optimal composition for the CO oxidation reaction.

Our calculations predict that Ge alloying induces both ligand and bifunctional effects. Charge transfer phenomena and orbital hybridization between Pt and Ge alters the adsorption properties of the catalyst (structure-activity relationship) in a composition dependent fashion. Further, Pt–Ge shows a dual adsorption behavior where CO always binds to Pt sites, while oxygen shows a clear preference towards Ge due to its greater oxophilicity. Precisely, this oxophilicity of Ge makes part of it oxidize to GeO_x, and consequently, a new oxygen source is developed resistant to CO poisoning. The provided results require a more thorough analysis to correctly sample the boundary between the CO poisoning and CO poisoning-free regimes as a function of pressures and temperature. As for now, this remains yet a topic of future study.

On the basis of this work, we believe that Ge alloying can be used for tuning the properties of Pt for catalytic applications. The high CO poisoning resistance conferred by Ge alloying without harming the catalytic activity makes it very appealing for industrial applications such as the water-gas shift reaction and hydrogen fuel cells.

Supporting Information

The authors have cited additional references within the Supporting Information (Ref. [73,74]).

Acknowledgements

A.U. gratefully thanks Eusko Jaurlaritza for his predoctoral grant and for his mobility grant EGONLABUR for short term stays. This work was supported by Grant No. PID2020-114754GA-I00 was funded by MCIN/AEI/10.13039/501100011033, and funding was provided by Gobierno Vasco-Eusko Jaurlaritza (Grant No. IT1254-19, IT1553-22). M.M.M. was supported by the Research Council of Finland (grant number 338228). DIPC and SGI-IZO-SGIker (UPV/EHU) are acknowledged for their technical support and the generous allocation of computational resources. The authors thankfully acknowledge also the computer resources at MareNostrum and the technical support provided by the Barcelona Supercomputing Center (Grant No. QHS-2022-2-002 and QHS-2022-3-0015).

Conflict of Interests

The authors declare no competing financial interest.

Data Availability Statement

The primary data that support the findings of this study are available within the article; additional data are available from the corresponding author upon reasonable request.

Keywords: bifunctional catalyst · CO oxidation · CO poisoning · Ge alloying · microkinetic modeling

[1] H.-J. Freund, G. Meijer, M. Scheffler, R. Schlögl, M. Wolf, *Angew. Chem. Int. Ed.* **2011**, *50*, 10064–10094.
[2] N. K. Soliman, *J. Mater. Res. Technol.* **2019**, *8*, 2395–2407.
[3] T. Engel, G. Ertl, in *Adv. Catal.* (Eds.: D. D. Eley, H. Pines, P. B. Weez), Academic Press, **1979**, pp. 1–78.
[4] A. K. Santra, D. W. Goodman, *Electrochim. Acta* **2002**, *47*, 3595–3609.
[5] S. Royer, D. Duprez, *ChemCatChem* **2011**, *3*, 24–65.
[6] P.-A. Carlsson, M. Skoglundh, P. Thormählen, B. Andersson, *Top. Catal.* **2004**, *30*, 375–381.
[7] C. H. Bartholomew, *Appl. Catal. Gen.* **2001**, *212*, 17–60.
[8] A. D. Allian, K. Takanabe, K. L. Fujdala, X. Hao, T. J. Truex, J. Cai, C. Buda, M. Neurock, E. Iglesia, *J. Am. Chem. Soc.* **2011**, *133*, 4498–4517.
[9] E. Jimenez-Izal, A. N. Alexandrova, *Annu. Rev. Phys. Chem.* **2018**, *69*, 377–400.
[10] E. Jimenez-Izal, B. C. Gates, A. N. Alexandrova, *Phys. Today* **2019**, *72*, 38–43.
[11] L. Liu, A. Corma, *Chem. Rev.* **2018**, *118*, 4981–5079.
[12] A. Halder, L. A. Curtiss, A. Fortunelli, S. Vajda, *J. Chem. Phys.* **2018**, *148*, 110901–110915.
[13] A. Beniya, S. Higashi, N. Ohba, R. Jinnouchi, H. Hirata, Y. Watanabe, *Nat. Commun.* **2020**, *11*, 1888–1897.
[14] F. Wang, Z. Li, H. Wang, M. Chen, C. Zhang, P. Ning, H. He, *Nano Res.* **2022**, *15*, 452–456.
[15] R. H. Lavroff, H. W. T. Morgan, Z. Zhang, P. Poths, A. N. Alexandrova, *Chem. Sci.* **2022**, *13*, 8003–8016.

[16] Z. Zhang, B. Zandkarimi, A. N. Alexandrova, *Acc. Chem. Res.* **2020**, *53*, 447–458.
[17] B. Zandkarimi, A. N. Alexandrova, *WIREs Comput. Mol. Sci.* **2019**, *9*, 1420–1436.
[18] S. M. M. Ehteshami, S. H. Chan, *Electrochim. Acta* **2013**, *93*, 334–345.
[19] E.-Y. Ko, E. D. Park, K. W. Seo, H. C. Lee, D. Lee, S. Kim, *Catal. Lett.* **2006**, *110*, 275–279.
[20] R. Mandapaka, S. Bachu, C. Srivastava, G. Madras, *Ind. Eng. Chem. Res.* **2017**, *56*, 8465–8473.
[21] J. Yin, J. Wang, T. Zhang, X. Wang, *Catal. Lett.* **2008**, *125*, 76–82.
[22] A. E. Aksoylu, M. M. A. Freitas, J. L. Figueiredo, *Catal. Today* **2000**, *62*, 337–346.
[23] B. S. Caglayan, İ. I. Soykal, A. E. Aksoylu, *Appl. Catal. B* **2011**, *106*, 540–549.
[24] S. Y. Chin, O. S. Alexeev, M. D. Amiridis, *J. Catal.* **2006**, *243*, 329–339.
[25] T. Ebashi, Y. Ishida, Y. Nakagawa, S. Ito, T. Kubota, K. Tomishige, *J. Phys. Chem. C* **2010**, *114*, 6518–6526.
[26] M. J. Lee, J. S. Kang, Y. S. Kang, D. Y. Chung, H. Shin, C.-Y. Ahn, S. Park, M.-J. Kim, S. Kim, K.-S. Lee, Y.-E. Sung, *ACS Catal.* **2016**, *6*, 2398–2407.
[27] T. F. Garetto, A. Borgna, C. R. Apesteguía, *Stud. Surf. Sci. Catal.* **1996**, *101*, 1155–1164.
[28] V. A. Mazzieri, C. L. Pieck, C. R. Vera, J. C. Yori, J. M. Grau, *Appl. Cat. Gen.* **2009**, *353*, 93–100.
[29] R. Mariscal, J. L. G. Fierro, J. C. Yori, J. M. Parera, J. M. Grau, *Appl. Cat. Gen.* **2007**, *327*, 123–131.
[30] Y. Ma, S. Song, C. Liu, L. Liu, L. Zhang, Y. Zhao, *Nat. Catal.* **2023**, *6*, 506–518.
[31] E. Jimenez-Izal, J.-Y. Liu, A. N. Alexandrova, *J. Catal.* **2019**, *374*, 93–100.
[32] P. Poths, G. Li, T. Masubuchi, H. W. T. Morgan, Z. Zhang, A. N. Alexandrova, *ACS Catal.* **2023**, *13*, 1533–1544.
[33] P. Poths, B. Zandkarimi, A. N. Alexandrova, E. Jimenez-Izal, *ChemCatChem* **2023**, *15*, 202201533–202201542.
[34] S. Rimaz, L. Chen, S. Kawi, A. Borgna, *Appl. Cat. Gen.* **2019**, *588*, 117266–117275.
[35] S. Rimaz, L. Chen, A. Monzón, S. Kawi, A. Borgna, *J. Chem. Eng.* **2021**, *405*, 126656–126655.
[36] S. Rimaz, M. Kosari, L. Chen, S. Xi, A. Monzón, S. Kawi, *Appl. Cat. Gen.* **2022**, *643*, 118751–118761.
[37] N. S. Veizaga, V. I. Rodriguez, M. Bruno, S. R. Miguel, *Electrocatalysis* **2019**, *10*, 125–133.
[38] E. M. Crabb, M. K. Ravikumar, *Electrochim. Acta* **2001**, *46*, 1033–1041.
[39] N. S. Veizaga, V. A. Paganin, T. A. Rocha, O. A. Scelza, S. R. Miguel, E. R. Gonzalez, *Int. J. Hydrogen Energy* **2014**, *39*, 8728–8737.
[40] H. P. Bideberripe, J. M. Ramallo-López, S. J. A. Figueroa, M. A. Jaworski, M. L. Casella, G. J. Siri, *Catal. Commun.* **2011**, *12*, 1280–1285.
[41] S. Zhou, X. Yang, Y. Shen, R. B. King, J. Zhao, *J. Alloys Compd.* **2019**, *806*, 698–704.
[42] A. Ugartemendia, K. Peeters, P. Ferrari, A. de Cózar, J. M. Mercero, E. Janssens, E. Jimenez-Izal, *ChemPhysChem* **2021**, *22*, 1603–1610.
[43] A. Ugartemendia, J. M. Mercero, A. de Cózar, E. Jimenez-Izal, *J. Chem. Phys.* **2022**, *156*, 174301–174311.
[44] J. P. Perdew, K. Burke, M. Ernzerhof, *Phys. Rev. Lett.* **1996**, *77*, 3865–3868.
[45] J. P. Perdew, K. Burke, M. Ernzerhof, *Phys. Rev. Lett.* **1997**, *78*, 1396–1396.
[46] G. Kresse, D. Joubert, *Phys. Rev. B* **1999**, *59*, 1758–1775.
[47] G. Kresse, J. Hafner, *Phys. Rev. B* **1993**, *47*, 558–561.
[48] G. Kresse, J. Hafner, *Phys. Rev. B* **1994**, *49*, 14251–14269.
[49] G. Kresse, J. Furthmüller, *Comput. Mater. Sci.* **1996**, *6*, 15–50.
[50] G. Kresse, J. Furthmüller, *Phys. Rev. B* **1996**, *54*, 11169–11186.
[51] S. Grimme, J. Antony, S. Ehrlich, H. Krieg, *J. Chem. Phys.* **2010**, *132*, 154104–154122.
[52] H. Zhai, A. N. Alexandrova, *J. Chem. Theory Comput.* **2016**, *12*, 6213–6226.
[53] G. Henkelman, B. P. Uberuaga, H. Jónsson, *J. Chem. Phys.* **2000**, *113*, 9901–9904.
[54] G. Henkelman, H. Jónsson, *J. Chem. Phys.* **2000**, *113*, 9978–9985.
[55] G. Henkelman, H. Jónsson, *J. Chem. Phys.* **1999**, *111*, 7010–7022.
[56] A. Heyden, A. T. Bell, F. J. Keil, *J. Chem. Phys.* **2005**, *123*, 224101–224115.
[57] A. H. Motagamwala, J. A. Dumesic, *Chem. Rev.* **2021**, *121*, 1049–1076.
[58] B. W. J. Chen, L. Xu, M. Mavrikakis, *Chem. Rev.* **2021**, *121*, 1007–1048.
[59] M. M. Kauppinen, M. M. Melander, A. S. Bazhenov, K. Honkala, *ACS Catal.* **2018**, *8*, 11633–11647.
[60] N. M. Alghamdi, R. Gautam, J. Gascon, D. G. Vlachos, S. M. Sarathy, *React. Chem. Eng.* **2022**, *7*, 2497–2507.
[61] R. D. Cortright, J. A. Dumesic, in *Adv. Catal.*, Academic Press, **2001**, pp. 161–264.
[62] A. Nilsson, L. G. M. Pettersson, *Surf. Sci. Rep.* **2004**, *55*, 49–167.
[63] J.-X. Liu, I. A. W. Filot, Y. Su, B. Zijlstra, E. J. M. Hensen, *J. Phys. Chem. C* **2018**, *122*, 8327–8340.
[64] J. C. González-Torres, V. Bertin, E. Poulain, O. Olvera-Neria, *J. Mol. Model.* **2015**, *21*, 279–288.
[65] L. Ma, M. Melander, T. Weckman, K. Laasonen, J. Akola, *J. Phys. Chem. C* **2016**, *120*, 26747–26758.
[66] L. Ma, K. Laasonen, J. Akola, *J. Phys. Chem. C* **2017**, *121*, 10876–10886.
[67] M. Di, K. Simmance, A. Schaefer, Y. Feng, F. Hemmingsson, M. Skoglundh, T. Bell, D. Thompsett, L. I. Ajakaiye Jensen, S. Blomberg, P.-A. Carlsson, *J. Catal.* **2022**, *409*, 1–11.
[68] S. Johansson, L. Österlund, B. Kasemo, *J. Catal.* **2001**, *201*, 275–285.
[69] L. Skubic, D. Kopač, B. Likozar, M. Huš, *Appl. Surf. Sci.* **2022**, *601*, 154135–154149.
[70] Y. Yang, S. K. Achar, J. R. Kitchin, *AIChE J.* **2022**, *68*, e17653.
[71] C. T. Campbell, *ACS Catal.* **2017**, *7*, 2770–2779.
[72] L. M. Molina, C. Arranz-Simón, J. A. Alonso, *J. Mol. Catal.* **2022**, *533*, 112749–112758.
[73] E. Jimenez-Izal, H. Zhai, J.-Y. Liu, A. N. Alexandrova, *ACS Catal.* **2018**, *8*, 8346–8356.
[74] E. Jones, T. Oliphant, P. Peterson, **2001**. Scientific computing in Python (SciPy). https://scipy.org/, [online; accessed 29.05.2023].

Manuscript received: September 11, 2023
Revised manuscript received: October 26, 2023
Accepted manuscript online: October 27, 2023
Version of record online: January 11, 2024